JAMES | Journal of Advances in Modeling Earth Systems

RESEARCH ARTICLE
10.1029/2019MS001617

Competing Effects of Droplet Sedimentation and Wind Shear on Entrainment in Stratocumulus

Bernhard Schulz[1] **and Juan Pedro Mellado**[1]

[1]Max-Planck-Institut für Meteorologie, Hamburg, Germany

Key Points:
- Submeter-scale resolution is necessary to appropriately represent the importance of droplet sedimentation on cloud top dynamics
- Entrainment reduction by droplet sedimentation can completely compensate entrainment enhancement by wind shear
- A better characterization of the droplet size distribution is needed to accurately represent mixing effects on cloud lifetime

Correspondence to:
B. Schulz,
bernhard.schulz@mpimet.mpg.de

Citation:
Schulz, B., & Mellado, J. P. (2019). Competing effects of droplet sedimentation and wind shear on entrainment in stratocumulus. *Journal of Advances in Modeling Earth Systems*, *11*, 1830–1846. https://doi.org/10.1029/2019MS001617

Received 22 JAN 2019
Accepted 15 MAY 2019
Accepted article online 20 MAY 2019
Published online 25 JUN 2019

Abstract The joint effect of droplet sedimentation and wind shear on cloud top entrainment in stratocumulus is investigated with direct numerical simulations. Although it is well understood that droplet sedimentation weakens entrainment while wind shear enhances entrainment, there is no consensus on the magnitude of each process. We find that the entrainment reduction by droplet sedimentation is sufficiently strong to completely compensate the entrainment enhancement by wind shear, and thus, droplet sedimentation and wind shear effects can be equally important for cloud top entrainment. For instance, for the subtropical conditions considered here, droplet sedimentation weakens entrainment by up to 40% while wind shear enhances entrainment by up to 40%. This result implies that the droplet size distribution can substantially affect cloud lifetimes not only because of its effect on rain formation but also because of its effect on cloud top entrainment, which emphasizes the need for a better characterization of droplet size distributions in stratocumulus. A second implication is that entrainment velocity parametrizations should pay equal attention to droplet sedimentation and to wind shear effects.

1. Introduction

Due to their net cooling effect and large area coverage, stratocumulus clouds are key for the Earth's radiation balance. However, predicting the lifetime of stratocumulus remains a challenge, partly because of the difficulty to quantify the interaction of the various processes that compound cloud top entrainment (Mellado, 2017; Stevens, 2005; Wood, 2012). In this work, we study the interaction of two processes involved in cloud top entrainment, namely, droplet sedimentation and cloud top wind shear.

Droplet sedimentation and cloud top wind shear can substantially alter cloud top entrainment, and they do it in opposite ways. Droplet sedimentation removes droplets from the entrainment interfacial layer (EIL) thus leaving behind warmer and dryer air. Consequently, droplet sedimentation reduces entrainment directly by inducing an upward sedimentation buoyancy flux and indirectly by reducing evaporative cooling (e.g., Ackerman et al., 2004, 2009; Bretherton et al., 2007; de Lozar & Mellado, 2017; Hill et al., 2009). Meanwhile, wind shear enhances the mixing between free tropospheric air and cloudy air, which increases entrainment directly by increasing the downward turbulent buoyancy flux and indirectly by enhancing evaporative cooling (e.g., Driedonks & Duynkerke, 1989; Katzwinkel et al., 2012; Kopec et al., 2016; Mellado et al., 2014; Schulz & Mellado, 2018; Wang et al., 2012). (The different fluxes and the evaporative cooling contribution are defined and analyzed in section 4.) These opposing effects raise the question whether droplet sedimentation and wind shear effects can compensate each other. We address this question here by means of direct numerical simulations (DNSs).

An important aspect is the representation of motions at meter and submeter scales. While studies based on large eddy simulations (LESs) report a sedimentation-induced reduction of the entrainment velocity of only 3–25% (Ackerman et al., 2009; Bretherton et al., 2007; Hill et al., 2009), a study based on DNSs indicates that sedimentation effects can be 2 to 3 times stronger (de Lozar & Mellado, 2017). This discrepancy is attributed to the size of the smallest resolved scales. The mixing length scale that is physically relevant is on the order of 1 m or less, larger scales being dominated by wave-like motions, which do not mix scalars very efficiently, and smaller scales being dominated by turbulent motions, which mix scalars very efficiently (the Ozmidov scale; see review by Mellado et al., 2018). Downgradient turbulence models represent wave-like motions very poorly and tend to overestimate the mixing of scalars, which explains why LES with grid spacings of 5 m overestimate the upward mixing of liquid water at the cloud top and thereby artificially compensate sedimentation effects. Numerical diffusion aggravates this problem. In contrast, DNS with grid spacings

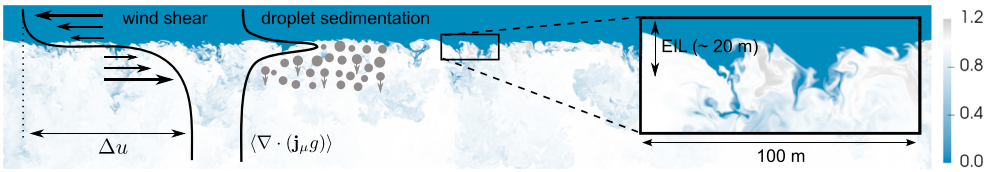

Figure 1. Vertical cross section of the simulated cloud top mixing layer showing the liquid water specific humidity field q_ℓ normalized by its in-cloud value q_ℓ^c. The mean velocity profile $\langle u \rangle$ and the mean profile of the divergence of the sedimentation buoyancy flux $\langle \nabla \cdot (\mathbf{j}_\mu g) \rangle$ is added for reference (cf. section 4). The entrainment interfacial layer (EIL) is located in the cloud top region and is a transition layer between cloudy and free tropospheric air (cf. section 3.2). Presented is the case $Sh_0 = 10$, $Sv_0 = 0$, and $Re_0 = 400$ at $z_*/\lambda = 16$.

on the order of 0.5 m allows to resolve the mixing length scales that are physically relevant (de Lozar & Mellado, 2017; Mellado et al., 2018). Using this high resolution shows that the reduction of the entrainment velocity by droplet sedimentation is about 40% (de Lozar & Mellado, 2017), which is comparable to the shear enhancement of the entrainment velocity observed by Schulz and Mellado (2018). This suggests that both processes can indeed compensate each other.

Another important aspect of the analysis of entrainment is the strong vertical variations of the EIL properties. This is particularly relevant for the study of the mean entrainment velocity, where entrainment velocity contributions from radiative cooling, evaporative cooling, and turbulent mixing can have order-of-one variations over the few meters that separate the reference heights typically used in the analysis of entrainment, such as the height of minimum turbulent buoyancy flux or the height of maximum mean buoyancy gradient (see discussion in Schulz & Mellado, 2018). Hence, in this work, we also investigate how the relative importance of droplet sedimentation and cloud top wind shear depends on this choice of the reference height.

This paper is structured as follows. Section 2 introduces the cloud top mixing layer (CTML) and discusses the simulation setup. Section 3 introduces some fundamental quantities which characterize the vertical structure of the CTML and in particular discusses sedimentation and shear effects on the EIL. Finally, section 4 investigates whether sedimentation and shear effects on the entrainment velocity can compensate each other. A summary of the results is given in section 5.

2. Simulation Setup

We use DNSs of the CTML to assess the combined effect of droplet sedimentation and wind shear on cloud top entrainment. The CTML mimics the upper part of a stratocumulus topped boundary layer and consists of a layer of relatively warm and dry air, representing the free troposphere, and a layer of relatively cold and moist air, representing the cloud layer below (see Figure 1). The simplified setup of the CTML neglects the effect of the large-scale motions with sizes of the order of the boundary layer depth. This simplification allows us to resolve the meter- and submeter-scale mixing processes that are important for sedimentation and shear effects on cloud top entrainment (cf. Table 1), complementing thereby previous LES studies where typical grid spacings are on the order of several meters (Mellado et al., 2018).

The formulation of the CTML is identical to the one used in de Lozar and Mellado (2017), where sedimentation effects alone are studied by means of DNSs. Here, we extend this work by additionally imposing cloud top wind shear. Droplet sedimentation effects are represented by means of a bulk microphysics scheme which is similar to previous LES studies by Ackerman et al. (2004) and Bretherton et al. (2007). Besides, inertial effects are neglected, since they are negligibly small for the conditions considered in this study (de Lozar & Mellado, 2014; Mellado, 2017). For conciseness, the formulation of the CTML is provided in de Lozar & Mellado (2014) and de Lozar & Mellado (2017), and this section only includes the discussion of the relevant nondimensional parameters and variables that are needed for the discussion of the results. A nondimensional formulation proves convenient to reduce the degrees of freedom in the parameter space that defines the problem and avoid redundancy of numerical experiments, to facilitate the generalization of results to other physical conditions, as well as to gain some a priori insight into the relative importance of the different processes considered in the study.

Table 1
Simulation Details

Sh_0	Sv_0	Sv_b	Re_0	Grid	L_x/λ	Δu (m/s)	η (cm)	z_* (m)	w_* (m/s)	h_{EIL} (m)	Ri_*	Ri_{Sh_0}
0	0.0	0.0	400	a	54	0.0	22	180	0.61	8.5	109	—
0	0.0	0.0	400	b	108	0.0	22	240	0.60	8.4	113	—
0	0.043	0.064	400	a	54	0.0	22	180	0.61	9.4	113	—
0	0.1	0.15	400	a	54	0.0	23	180	0.58	11.3	124	—
5	0.0	0.0	400	a	54	1.5	21	180	0.61	9.2	109	1.0
5	0.043	0.064	400	a	54	1.5	22	180	0.59	10.3	118	1.1
5	0.1	0.15	400	a	54	1.5	23	180	0.58	12.1	120	1.3
10	0.0	0.0	400	a	54	3.1	20	180	0.62	13.8	106	0.4
10	0.0	0.0	400	b	108	3.1	20	240	0.62	14.0	107	0.4
10	0.043	0.064	400	a	54	3.1	21	180	0.60	14.2	113	0.4
10	0.1	0.15	400	d	108	3.1	22	200	0.58	14.8	122	0.4
0	0.0	0.0	1,200	c	54	0.0	10	130	0.53	4.6	105	—
10	0.0	0.0	800	c	54	3.1	12	130	0.54	10.4	100	0.3
10	0.1	0.15	800	c	54	3.1	13	130	0.49	11.5	119	0.3

Note. $Sh_0 = \Delta u/U_0$ defines the shear number; $Sv_0 = u_{\mathrm{sed}}/U_0$ defines the sedimentation number; Sv_b defines the buoyancy sedimentation number (cf. equation (5)); $Re_0 = (\lambda U_0)/\nu$ defines the reference Reynolds number; grid (a) corresponds to $2,560^2 \times 1,408$; grid (b) to $5,120^2 \times 1,792$; grid (c) to $5,120^2 \times 2,048$; grid (d) to $5,376^2 \times 1,792$; L_x is the horizontal domain size; λ is the extinction length (with $\lambda = 15$ m); Δu is the cloud top velocity jump; η is the Kolmogorov scale; z_* is the convective length scale; w_* is the convective velocity scale; h_{EIL} is the thickness of the EIL; $Ri_* = z_* \Delta b / w_*^2$ is the convective Richardson number; and $Ri_{\mathrm{Sh}_0} = h_{\mathrm{EIL}}/(3h_{\mathrm{Sh}_0}) = h_{\mathrm{EIL}}\Delta b/(\Delta u)^2$ is the shear Richardson number. The value of z_* indicates the final time considered in the analysis (cf. section 2.2), and all other time-dependent variables (columns 10–13) are averaged over the period $10 < z_*/\lambda < 12$ for $Re_0 = 400$ and over the period $7.5 < z_*/\lambda < 8.5$ for $Re_0 > 400$. EIL = entrainment interfacial layer.

2.1. Dimensional Analysis

The liquid water mass flux due to the gravitational settling of the cloud droplets, or sedimentation flux, can be written as (cf., de Lozar & Mellado, 2014, 2017)

$$\rho \mathbf{j}_\mu = -\pi (108\mu_{\mathrm{g}})^{-1} \rho_\ell^2 N_{\mathrm{d}} \overline{d^5} g \mathbf{k}, \tag{1}$$

where ρ is the density of the fluid, μ_g is the dynamic viscosity of the environmental air, ρ_ℓ is the density of liquid water, N_{d} is the droplet number density, $\overline{d^n}$ is the nth moment of the droplet size distribution (DSD), g is the magnitude of the gravitational acceleration, and $\mathbf{k}$ is a unit vector pointing upward in the vertical direction. The dependence of the sedimentation flux on the DSD fifth moment results from the product of the mass of the droplet, proportional to the droplet's volume, and the Stokes terminal velocity, proportional to the droplet's area. This dependence indicates the importance of the large droplets or the tail of the DSD. The sedimentation flux appears in the evolution equations of the total specific humidity q_t and the specific enthalpy h (de Lozar & Mellado, 2017). In addition, the sedimentation flux changes the density field and thus introduces a sedimentation buoyancy flux $-\mathbf{j}_\mu g$ in the evolution equation of the buoyancy, which can be an important contribution to the entrainment velocity, as discussed in section 4.

In the bulk microphysics scheme employed here, we follow previous work and assume a lognormal DSD and a constant droplet number density N_d (cf., Ackerman et al., 2004; Bretherton et al., 2007; de Lozar & Mellado, 2014, 2017). With this assumption and the Boussinesq approximation, the sedimentation flux per unit mass can be written as

$$\mathbf{j}_\mu = -q_\ell^{\mathrm{c}} u_{\mathrm{sed}} \left(\frac{q_\ell}{q_\ell^{\mathrm{c}}} \right)^{5/3} \mathbf{k}, \tag{2}$$

where q_ℓ is the liquid water specific humidity and q_ℓ^{c} its value within the interior of the cloud. Moreover,

$$u_{\mathrm{sed}} = g[(\rho_\ell d_{\mathrm{v}}^2)/(18\mu_g)] \exp[5(\log \sigma_{\mathrm{gc}})^2] \tag{3}$$

is a bulk sedimentation velocity. The volume mean droplet diameter in the cloud is defined as $d_{\mathrm{v}} \equiv (\overline{d^3})^{1/3} = (6\rho^{\mathrm{c}} q_\ell^{\mathrm{c}})^{1/3} (\pi \rho_\ell N_d)^{-1/3}$, where ρ^{c} denotes the density of cloudy air and σ_{gc} is the geometric standard deviation

of the log-normal DSD. A bulk value of the sedimentation velocity that includes the factor $\exp[5(\log\sigma_{gc})^2]$ is appropriate to represent the effect of the whole DSD and not only of one particular droplet size such as d_v, which is important because larger droplets contribute significantly to the sedimentation flux.

According to equation 2, the sedimentation flux can be fully characterized by two nondimensional parameters, namely, one related to the bulk settling velocity describing how fast the droplets fall and one related to the in-cloud liquid water content, that is, how much liquid mass is being transported. As the first nondimensional parameter, we consider the sedimentation number

$$Sv_0 = \frac{u_{\mathrm{sed}}}{U_0}, \tag{4}$$

where $U_0 = (B_0\lambda)^{1/3}$ is a reference radiative velocity scale. In this definition, λ is the extinction length scale, which characterizes the depth over which the radiative flux divergence concentrates, and $B_0 = R_0 g/(\rho^{\mathrm{c}} c_p^{\mathrm{c}} T^{\mathrm{c}})$ is the reference buoyancy flux that is associated with the reference longwave radiative cooling R_0 (de Lozar & Mellado, 2017; Mellado, 2017). In the definition of B_0, c_p^{c} and T^{c} are the specific heat capacity and temperature of cloudy air, respectively. Equation (4) illustrates the advantage of using nondimensional numbers, as a single sedimentation number Sv_0 characterizes various ratios of u_{sed} and U_0. As the second nondimensional parameter, we consider

$$Sv_b = \frac{q_\ell^{\mathrm{c}} u_{\mathrm{sed}}}{\beta B_0}\frac{g}{}, \tag{5}$$

which characterizes the sedimentation buoyancy flux (cf. de Lozar & Mellado, 2017) and which directly appears in the entrainment rate equation discussed in section 4. The parameter β is the fraction of radiatively induced enthalpy changes that translate into buoyancy changes.

Cloud top wind shear is characterized by the shear number

$$Sh_0 = \frac{\Delta u}{U_0}, \tag{6}$$

where $\Delta u = ||\mathbf{u}^{\mathrm{d}} - \mathbf{u}^{\mathrm{c}}||$ defines a constant jump of the horizontal velocity, with $\mathbf{u}^{\mathrm{d}}$ and $\mathbf{u}^{\mathrm{c}}$ being the mean horizontal velocity vectors in the dry free troposphere and within the cloud, respectively (a superscript "d" indicates dry free tropospheric air). The parameter Sh_0 completely characterizes wind shear effects in the CTML since we can always choose a reference frame which moves with the mean velocity $(\mathbf{u}^{\mathrm{d}} + \mathbf{u}^{\mathrm{c}})/2$ and which is aligned with the vector $\mathbf{u}^{\mathrm{d}} - \mathbf{u}^{\mathrm{c}}$.

In the phase equilibrium formulation adopted here, the buoyancy reversal parameter D, the mixture fraction at saturation conditions χ_{sat} and the parameter β introduced in equation (5) completely characterize the effect of phase changes in the water substance (cf. de Lozar & Mellado, 2017). The mixture fraction at saturation conditions is given by $\chi_{\mathrm{sat}} = (q_{\mathrm{t,sat}} - q_{\mathrm{t}}^{\mathrm{c}})/\Delta q_{\mathrm{t}}$, where $q_{\mathrm{t,sat}}$ is the total water specific humidity at saturation conditions and Δq_{t} is the cloud top jump in total water specific humidity. In addition, the buoyancy reversal parameter is defined as $D = -b_{\mathrm{sat}}/\Delta b$, that is, the ratio of the buoyancy at saturation conditions b_{sat} to the buoyancy jump across the cloud top $\Delta b = b^{\mathrm{d}} - b^{\mathrm{c}}$. Atmospheric conditions in which $D > 0$, such as in the simulations performed in this study, allow for buoyancy reversal instability (Deardorff, 1980b; Randall, 1980).

This set of nondimensional numbers is completed by a reference Richardson number $Ri_0 = \lambda\Delta b/U_0^2$, which characterizes the strength of the inversion against eddies of size λ and a reference Reynolds number $Re_0 = \lambda U_0/\nu$, which characterizes molecular diffusive effects. In summary, the set of nondimensional numbers $\{Sv_0, Sv_b, Sh_0, D, \chi_{\mathrm{sat}}, \beta, Ri_0, Re_0\}$ completely characterizes the CTML (see Table 1).

2.2. Description of Simulations

To assess the effect of droplet sedimentation and wind shear on cloud top entrainment, we fix all parameters according to the first research flight (RF01) of the DYCOMS-II flight campaign (Stevens et al., 2005) and vary only the sedimentation number Sv_0 and the shear number Sh_0. Major reference parameters for RF01 of DYCOMS-II are summarized in Table 2. These parameters are representative of subtropical conditions, where substantial jumps in total water specific humidity Δq_{t} and temperature ΔT are commonly found across the cloud top.

Table 2
List of Fixed Reference Parameters for RF01 of the DYCOMS-II Campaign

U_0	0.3 m/s	Reference velocity scale
B_0	1.9×10^{-3} m^2/s^3	Reference buoyancy flux
λ	15 m	Extinction length
Δb	0.25 m/s^2	Jump in buoyancy
Δq_t	−7.5 g/kg	Jump in total water specific humidity
ΔT	8.5 K	Jump in temperature
Ri_0	40.2	Reference Richardson number

Note. In addition, we set $\chi_{sat} = 0.09$, $\beta = 0.53$, $D = 0.031$, $T^c = 283.8$ K, and $q_\ell^c = 0.5 \mathrm{g\,kg^{-1}}$ (cf. section 2). The reference buoyancy flux B_0 corresponds to a reference longwave radiative cooling of $R_0 = 70$ W/m^2.

Regarding sedimentation effects, we investigate three cases, namely, a no-sedimentation case ($Sv_0 = 0$), a moderate sedimentation case ($Sv_0 = 0.043$), and a strong sedimentation case ($Sv_0 = 0.1$), as summarized in Table 1. Figure 2 presents contour plots of u_{sed} as a function of the volume mean droplet diameter d_v and as a function of the geometric standard deviation σ_{gc}. Droplet diameters are typically reported to be in the range of 10–30 μm (Ackerman et al., 2009; Glienke et al., 2017; Grosvenor et al., 2018; Haman et al., 2007; Katzwinkel et al., 2012; Martin et al., 1994; VanZanten et al., 2005), and the geometric standard deviation is reported to be in the range $\sigma_{gc} \simeq 1$–2 with the most probable value being on the order of $\sigma_{gc} \simeq 1.2$–1.5 (Ackerman et al., 2004; Bretherton et al., 2007; Grosvenor et al., 2018; Hudson & Yum, 1997; Miles et al., 2000; Martin et al., 1994; Pawlowska & Brenguier, 2000; VanZanten et al., 2005; Wood, 2000). For RF01 of DYCOMS-II one finds $d_v \simeq 20$ μm (i.e., $N_d = 140$ cm^{-1}) and $\sigma_{gc} = 1.2$ as most probable values (Bretherton et al., 2007; VanZanten et al., 2005), even though Ackerman et al. (2004) used $\sigma_{gc} = 1.5$ for the very same case. The cases $Sv_0 = 0.043$ and $Sv_0 = 0.1$ are designed to investigate this sensitivity in σ_{gc}, where $Sv_0 = 0.043$ approximates the pair $\{d_v \simeq 20$ μm, $\sigma_{gc} = 1.2\}$ and $Sv_0 = 0.1$ the pair $\{d_v \simeq 20$ μm, $\sigma_{gc} = 1.5\}$. According

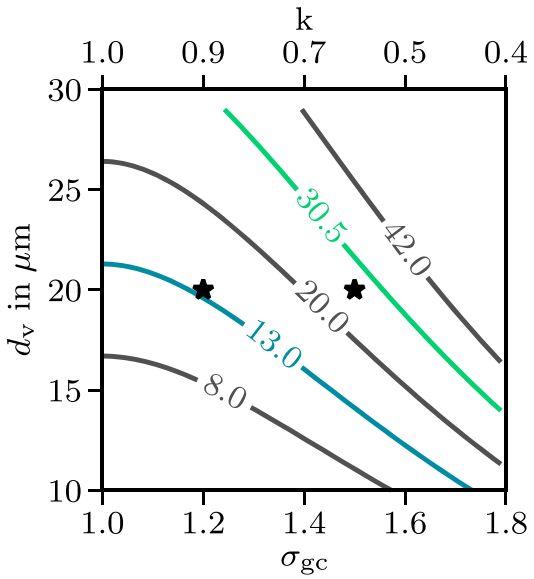

Figure 2. Contour plot of the bulk sedimentation velocity u_{sed} in millimeter per second as function of the volume mean droplet diameter d_v and the geometric standard deviation σ_{gc}. The second horizontal axis at the top shows the related value of $k = (d_v/d_e)^3 = \exp[-3(\ln \sigma_{gc})^2]$, where $d_e = \overline{d^3}/\overline{d^2}$ is the droplet effective diameter. The two black stars correspond to the reference cases $\{\sigma_{gc} \simeq 1.2, d_v \simeq 20\,\mu$m$\}$ and $\{\sigma_{gc} \simeq 1.2, d_v \simeq 20\,\mu$m$\}$, which are approximated by the sedimentation number Sv_0=0.043 (blue contour line) and the Sv_0=0.1 (green contour line) respectively.

to equation (4), these values correspond to a bulk sedimentation velocity of $u_{\mathrm{sed}} \simeq 13$ mm/s and $u_{\mathrm{sed}} \simeq 30.5$ mm/s. The exponential factor in equation (3) explains why these values are larger than the sedimentation velocities obtained for single droplets, which are typically on the order of 3–12 mm/s (e.g., Mellado, 2017).

Regarding the second settling parameter, one finds $Sv_b \simeq 1.5\,Sv_0$ for RF01 of DYCOMS-II (cf. Table 1). According to equation (5), an estimate for the corresponding magnitude of the sedimentation buoyancy flux $-\mathbf{j}_\mu g$ is 0.06–0.15 $\times 10^{-3}$ m^2/s^3. This estimate shows that the sedimentation buoyancy flux can be a 20% contribution to the entrainment buoyancy flux, which is estimated as $w_e \Delta b \simeq 0.75 \times 10^{-3}$ m^2/s^3 when using an entrainment velocity of 3 mm/s and a buoyancy jump of 0.25 m/s^2 (see Appendix C). This estimate already indicates the relevance of the sedimentation buoyancy flux for altering entrainment rates.

To determine the sensitivity of cloud top entrainment to wind shear, we consider three shear numbers Sh_0 (for each value of Sv_0): A no-shear case ($Sh_0 = 0$), a moderate shear case ($Sh_0 = 5$), and a strong shear case ($Sh_0 = 10$), as summarized in Table 1. These shear numbers correspond to cloud top velocity jumps in the range of $\Delta u = 0$–3.1 m/s. The largest jump of $\Delta u = 3.1$ m/s represents typical atmospheric conditions, as most cloud top velocity jumps are reported to be on the order of $\Delta u = 4$ m/s, although extreme values of up to $\Delta u = 10$ m/s have occasionally been observed (Brost et al., 1982; Faloona et al., 2005; Katzwinkel et al., 2012; Malinowski et al., 2013; Nicholls & Leighton, 1986; de Roode & Wang, 2007).

This discussion shows that we match all parameters of RF01 of DYCOMS-II except the Reynolds number, which implies that we need to investigate the sensitivity of our results to changes in the Reynolds number. Sensitivity studies presented in Appendix A reveal that the properties discussed in this paper depend only weakly on the Reynolds number; in particular, increasing the Reynolds number by a factor of 2 changes the mean entrainment velocity (defined in equation (12)) by less than 20%. These findings indicates that we start to reach Reynolds numbers that are large enough to observe some degree of Reynolds number similarity (Dimotakis, 2005; Mellado et al., 2018), which justifies the use of DNS for studying some aspects of cloud top entrainment in stratocumulus.

The grid spacing is isotropic and uniform within the region where the turbulent flow develops. The ratio of the grid spacing to the Kolmogorov scale η is approximately 1.5, which implies a grid spacing of 20 cm to 32 cm (depending on Re_0; see Table 1). With this configuration, we reach submeter-scale resolution since the compact schemes used in this study allow representing the transfer function of first-derivative operators with a 99% accuracy using four grid points per wavelength (e.g., see the numerical analysis in Lele, 1992). In addition, the ratio of the horizontal domain size L_x to the convective length scale z_* needs to be large enough for our results to become independent of L_x (Bailon-Cuba et al., 2010; Mellado, 2012). The convective length scale z_* characterizes the vertical extent of the turbulent flow and is defined by equation (7) and further explained in section 3.1. The ratio L_x/z_* diminishes as z_* grows in time, and at the end of our simulations we reach $L_x/z_* \simeq 4.5$ for grid (a), $L_x/z_* \simeq 6.5$ for grids (b) and (c), and $L_x/z_* \simeq 8$ for grid (d). A sensitivity study based on the cases $\{Sh_0 = 0, Sv_0 = 0\}$ and $\{Sh_0 = 10, Sv_0 = 0\}$ shows that the ratio of $L_x/z_* \simeq 4.5$ is sufficient for the statistics that we study to become approximately independent of L_x. This result is obtained by observing that statistics at $z_*/\lambda \simeq 12$ using grid (a), where $L_x/z_* \simeq 4.5$, are similar to those obtained using grid (b), where $L_x/z_* \simeq 9$. Using grids (b) and (d) improves the statistical convergence when considering the temporal evolution of horizontal averages, and it allows us to run the simulations over a longer interval of z_*/λ, which proves convenient for studying scaling laws. The cases with the large grids, namely, grids (b)–(d) are computationally very expensive and for that reason we only run them up to $L_x/z_* \simeq 6.5$ and $L_x/z_* \simeq 8$ respectively, which corresponds to $z_* \simeq 240$ m for grid (b), to $z_* \simeq 130$ m for grid (c), and to $z_* \simeq 200$ m for grid (d). Further details regarding the simulations are given in de Lozar and Mellado (2015b, 2017) and Mellado et al. (2014), and further details regarding the numerical algorithm are given in Mellado, (2010) and Mellado & Ansorge (2012).

3. Droplet Sedimentation and Wind Shear Effects on the Vertical Structure

This section characterizes in-cloud properties of the performed simulations by introducing convective scalings and characterizes cloud top properties by discussing droplet sedimentation and wind shear effects on the EIL. We show that droplet sedimentation and wind shear can alter cloud top properties—like the thickness of the EIL—without significantly changing in-cloud properties further below.

3.1. In-Cloud Convective Scalings

In stratocumulus, turbulence is generated within the cloud top region by shear instabilities caused by the mean wind and by convective instabilities caused by evaporative and radiative cooling. Turbulence generation by wind shear tends to concentrate at the EIL, a relatively thin region below which free convection prevails. This suggests to introduce convective scalings in the analysis, which can be based on a convective length scale

$$z_* = B_{\max}^{-1} \int_{z_{-\infty}}^{z_{\infty}} \mathcal{H}(B)\mathrm{d}z \tag{7}$$

and a convective velocity scale

$$w_* = (B_{\max} \quad z_*)^{1/3}, \tag{8}$$

where $\mathcal{H}$ denotes the Heaviside function, $B = \langle w' b' \rangle$ is the turbulent buoyancy flux, and $B_{\max}$ its maximum within the cloud (Deardorff, 1980a; Mellado et al., 2014). The limits of integration in equation (7) are far enough below and above the cloud top region for z_* and w_* to be independent of them. The angle brackets $\langle \cdot \rangle$ indicate a horizontal average, and a prime indicates fluctuations. Note that the definition of w_* deviates by a factor $2.5^{1/3} \simeq 1.4$ from previous work (Deardorff, 1980a; Wood, 2012). The reason is that the CTML does not retain the subcloud layer, where the linear vertical variation of the buoyancy flux justifies a factor of 2.5.

As turbulence propagates downward the convective length scale, z_*, increases and we use this link between time and z_* to express the evolution of the system in terms of the nondimensional variable z_*/λ. This is convenient since the variable z_*/λ expresses the scale separation between the integral length scale z_*, associated with in-cloud turbulence, and the extinction length scale λ, associated with radiative cooling. An additional advantage of using z_*/λ is that it is directly linked to the in-cloud turbulent intensity w_* by means of equation (8). In our simulations we typically reach values of $z_*/\lambda \simeq$12–16 (cf. Table 1) and the initial transient takes roughly $z_*/\lambda \simeq 8$, that is, statistics for different initial conditions usually deviate by less than 15% for $z_*/\lambda > 8$ (not shown). We therefore focus on the regime $z_*/\lambda > 8$ in our analysis. To improve statistical convergence, a running mean with the period $z_*/\lambda = 2$ is applied to all results presented in the main text.

We observe that w_* is in the range of 0.5–0.6 m/s for all sedimentation and shear numbers investigated (cf. Table 2), which shows that w_* is insensitive toward changes in droplet sedimentation and wind shear. In other words, droplet sedimentation and wind shear effects can remain localized within the cloud top region and do not necessarily change in-cloud properties (see Schulz & Mellado, 2018, for details).

3.2. The EIL

The EIL refers to the region where warm and dry air from the free troposphere is mixed with cold and moist air from the cloud interior and thus defines a transition layer between the cloud and the free troposphere. (Part of the mixing takes place below the EIL as free tropospheric air is transported deep into the cloud interior through cloud holes, as observed in Figure 1 and as thoroughly studied by Gerber et al., 2005, 2016, but we do not focus on these cloud holes in the current analysis.) This implies that the EIL is characterized by strong vertical variations in temperature, buoyancy, and liquid water specific humidity. We follow previous work by Schulz and Mellado (2018) and define the EIL thickness, h_{EIL}, as

$$h_{\mathrm{EIL}} = z_{0.9\Delta b} - z_{\mathrm{i,n}}, \tag{9}$$

where $z_{0.9\Delta b}$ is the height where the mean buoyancy $\langle b \rangle$ reaches 90% of Δb and $z_{\mathrm{i,n}}$ denotes the height of zero mean buoyancy. With this definition the EIL is stably stratified and approximately coincides with the region where the turbulent buoyancy flux is negative (see Figure 3a). Our definition of the EIL closely follows the definition by Caughey et al. (1982) as the layer containing the majority of the temperature jump (buoyancy in our case), and $z_{\mathrm{i,n}}$ can be interpreted as the base of the capping inversion. However, our definition of the EIL differs from the definition proposed by Malinowski et al. (2013), especially regarding the lower boundary of the EIL, and this difference has to be taken into account when comparing results.

Our simulations show that droplet sedimentation and wind shear thicken the EIL. Sedimentation thickens the EIL by removing cloudy air from the EIL thus leaving behind warmer and dryer air. As a consequence, the mean buoyancy profile deforms in such a way that $z_{\mathrm{i,n}}$ moves downward with respect to $z_{0.9\Delta b}$, which thickens the EIL. However, the sedimentation-induced thickening of the EIL remains moderate, namely,

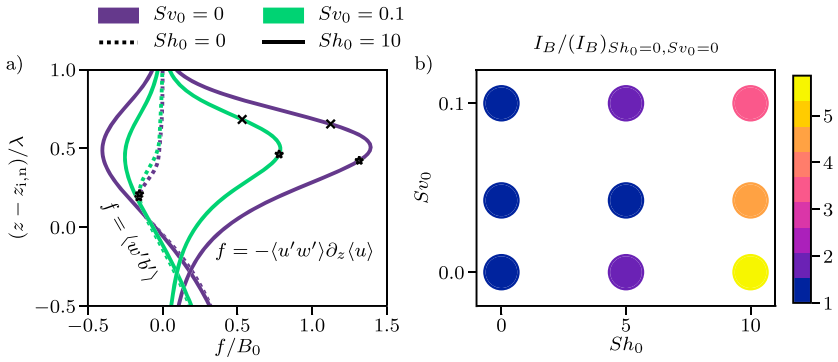

Figure 3. (a) Normalized turbulent buoyancy flux and normalized shear production term, where the different symbols indicate different reference heights: The star indicates the height of minimum turbulent buoyancy flux $z_{i,f}$, the cross the height of the maximum gradient of the mean buoyancy profile $z_{i,g}$, and the vertical distance z is plotted with respect to the height of zero mean buoyancy $z_{i,n}$. Colors indicate sedimentation numbers Sv_0, and line styles shear number Sh_0, for example, the dashed green line indicates the pair $\{Sv_0 = 0.1, Sh_0 = 0\}$. (b) Normalized rate of net turbulent kinetic energy consumption for entrainment, where I_B is defined as $I_B = \int_{z_{-\infty}}^{z_{+\infty}} B\mathcal{H}(-B)\mathrm{d}z$ and $B = \langle w'b'\rangle$. Both figures are presented for $Re_0 = 400$ at $z_*/\lambda \simeq 11$.

h_{EIL} increases by ~30% when the sedimentation number is increased from $Sv_0 = 0$ to $Sv_0 = 0.1$ for $Sh_0 = 0$ (see Table 1).

Shear-induced thickening of the EIL is frequently observed in literature (e.g., Katzwinkel et al., 2012; Jen-La Plante et al., 2016; Wang et al., 2008, 2012) and can be substantially stronger than the sedimentation-induced thickening of the EIL. However, shear-induced thickening is only observed once the cloud top velocity jump exceeds its critical value $(\Delta u)_{\mathrm{crit}}$=2.4-3.0 m/s (see equation (11)). In agreement with that, Table 2 shows that a strong shear characterized by $\{Sh_0 = 10, Sv_0 = 0.0\}$ thickens the EIL by ~70%, while a weak shear characterized by $\{Sh_0 = 5, Sv_0 = 0.0\}$ does not significantly thicken the EIL. The reason for this difference is that in the case $Sh_0 = 10$ the EIL thickness h_{EIL} is set by the width of the shear production term $P = -\langle u'w'\rangle\partial_z\langle u\rangle$, while in the case $Sh_0 = 5$ the EIL thickness h_{EIL} is set by the width of the turbulent transport term. By comparing these two different scalings for h_{EIL}, a critical cloud top velocity jump $(\Delta u)_{\mathrm{crit}}$ is derived in Schulz and Mellado (2018), where shear effects are argued to be significant for $\Delta u > (\Delta u)_{\mathrm{crit}}$ and negligible for $\Delta u < (\Delta u)_{\mathrm{crit}}$. This critical cloud top velocity jump is defined as

$$(\Delta u)_{\mathrm{crit}} \simeq \sqrt{\frac{3\alpha_1}{2\alpha_3^{-1} - 3\alpha_2}} w_* \,, \tag{10}$$

where w_* is the convective velocity defined in equation (8). The parameters α_1 and α_2 determine the amount of kinetic energy associated with an air parcel penetrating into the stably stratified EIL, while the parameter

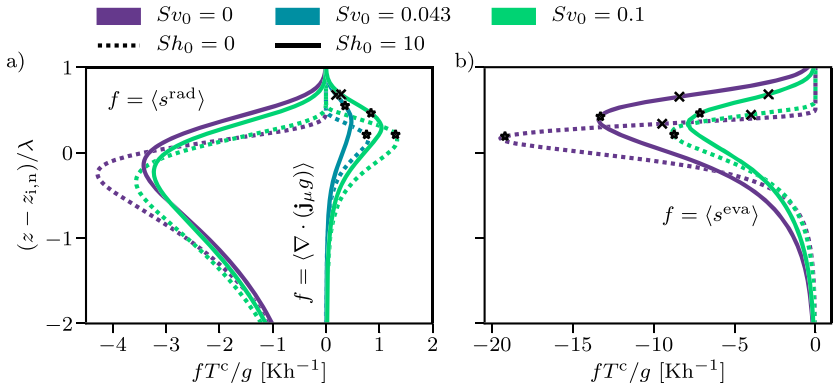

Figure 4. Mean profiles of the different buoyancy source terms according to equation (13), where the different symbols indicate different reference heights: The star indicates the height of minimum turbulent buoyancy flux $z_{i,f}$ and the cross the height of the maximum gradient of the mean buoyancy profile $z_{i,g}$. The vertical distance z is plotted with respect to the height of zero mean buoyancy, $z_{i,n}$, and the figure is presented for $Re_0 = 400$ at $z_*/\lambda \simeq 11$.

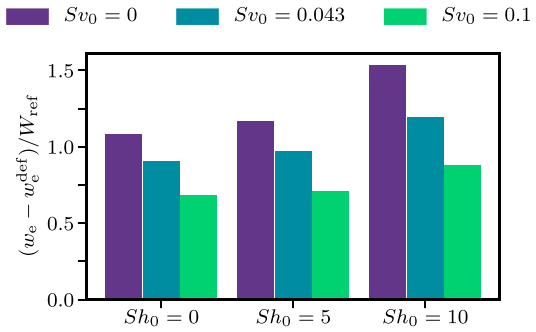

Figure 5. Normalized quasi-steady entrainment velocity $w_e - w_e^{def}$ (see equation (14)) evaluated at the height of zero mean buoyancy $z_{i,n}$ for $Re_0 = 400$ at $z_*/\lambda \simeq 11$. For each triplet the shear number Sh_0 is fixed and the sedimentation number Sv_0 is varied.

α_3 is related to the EIL thickness h_{EIL}, as discussed in Appendix B. We find that sedimentation modifies the set of parameters $\{\alpha_1, \alpha_2, \alpha_3\}$ only mildly, changing from $\{4.7, 0.60, 0.75\}$ for $Sv_0 = 0.0$ to $\{4.8, 0.56, 0.84\}$ for $Sv_0 = 0.043$ and to $\{5.3, 0.53, 0.90\}$ for $Sv_0 = 0.1$. Substituting these parameters into equation (10) yields a critical cloud top velocity jump in the range of

$$(\Delta u)_{crit} = 4 - 5w_* \,, \tag{11}$$

where the lower limit of $4w_*$ corresponds to $Sv_0 = 0.0$ and the upper limit of $5w_*$ to $Sv_0 = 0.1$. Hence, droplet sedimentation effects on the critical cloud top velocity jump $(\Delta u)_{crit}$ remain moderate, below 25%. Typical values of w_* are in the range $w_* \simeq$0.2–0.9 m/s (Wood, 2012), which implies typical critical velocity jumps in the range $(\Delta u)_{crit} \simeq$1–4 m/s. We reach $w_* \simeq$0.6 m/s at the end of the simulations (cf. Table 1), which corresponds to $(\Delta u)_{crit} = 2.4$–3.0 m/s. Therefore, only the strongest velocity jump with $\Delta u \simeq 3.1$ m/s ($Sh_0 = 10$) exceeds the critical shear velocity $(\Delta u)_{crit}$, which explains why shear effects in Figure 3, 5, and 6 are observed to be negligible for $\Delta u \lesssim 1.5$ m/s ($Sh_0 \lesssim 5$).

We further find that sedimentation-induced and shear-induced broadening of the EIL are not additive but partially compensate each other. As indicated in Table 1, imposing a strong shear broadens the EIL by ~ 6 m compared to the no-shear case, and imposing a strong sedimentation broadens the EIL by ~ 3 m compared to the no-sedimentation case, but simultaneously imposing a strong shear and a strong sedimentation broadens the EIL only by ~7 m compared to the no-shear and no-sedimentation case. To understand this behavior, recall that sedimentation thickens the EIL, which weakens the shear production term $P = -\langle u'w' \rangle \partial_z \langle u \rangle$. As a consequence, sedimentation weakens the maximum of the shear production term by approximately 40% and the net amount of turbulent kinetic energy used for entrainment by approximately 30%, as indicated in Figures 3a and 3b respectively. In this way, sedimentation diminishes the shear-induced thickening of h_{EIL} to approximately ~7 m instead of ~6 m + 3 m = 9 m. As argued in detail in Appendix B, this compensating effect of sedimentation and shear on the EIL thickness helps to explain why sedimentation effects on the critical velocity jump $(\Delta u)_{crit}$ remain moderate.

4. Droplet Sedimentation and Wind Shear Effects on the Entrainment Velocity

This section investigates the combined effect of droplet sedimentation and wind shear on the various contributions to the mean entrainment velocity w_e from mixing, radiative cooling, and evaporative cooling. This analysis provides evidence to our initial claim that droplet sedimentation and wind shear effects on the mean entrainment velocity w_e can compensate each other.

4.1. Mean Entrainment Velocity

Following Lilly (1968), we define the mean entrainment velocity as

$$w_e = \frac{dz_i}{dt} - \langle w \rangle_{z_i}, \tag{12}$$

where z_i defines a reference height marking the cloud top region, $\langle w \rangle_{z_i}$ is a mean vertical velocity, and a subscript z_i indicates that the corresponding quantity is evaluated at z_i. The choice of z_i is arbitrary, and different definitions of z_i have been proposed in literature (e.g., Malinowski et al., 2013; Schulz & Mellado, 2018). Here we consider three reference heights: The height of zero mean buoyancy $z_{i,n}$, the height of minimum turbulent buoyancy flux $z_{i,f}$, and the height of maximum gradient of the mean buoyancy profile $z_{i,g}$. According to equation (9) the reference height $z_{i,n}$ coincides with the lower end of the EIL, while the reference height $z_{i,g}$ is located near the upper end of the EIL (not shown). These different reference heights are only separated by a few meters, namely, $z_{i,n}$ lies 7–10 m below $z_{i,f}$, which in turn lies 3–6 m below $z_{i,g}$, as indicated in Figure 4 (with $\lambda \simeq$15 m). In agreement with previous work by Schulz and Mellado (2018) we show below that these small height differences are crucial for some quantities while being negligible for others.

Droplet sedimentation and wind shear effects on the mean entrainment velocity are analyzed in more detail by means of the entrainment rate equation, which analytically relates w_e to the sum of six contributions.

The entrainment rate equation is obtained by integrating the buoyancy evolution equation

$$D_t b = \kappa_T \nabla^2 b + \nabla \cdot (\mathbf{j}_\mu g) + s^{\mathrm{rad}} + s^{\mathrm{eva}} , \tag{13}$$

from an arbitrary reference height $z = z_i$ upward, where κ_T denotes the thermal diffusivity and $\nabla \cdot (\mathbf{j}_\mu\, \mathrm{g})$ a sedimentation buoyancy flux contribution. The radiative source term s^{rad} and the evaporative source term s^{eva} are defined in Appendix B. One obtains

$$w_{\mathrm{e}} = w_{\mathrm{e}}^{\mathrm{tur}} + w_{\mathrm{e}}^{\mathrm{sed}} + w_{\mathrm{e}}^{\mathrm{eva}} + w_{\mathrm{e}}^{\mathrm{rad}} + w_{\mathrm{e}}^{\mathrm{mol}} + w_{\mathrm{e}}^{\mathrm{def}} . \tag{14}$$

For conciseness, the exact definition of each contribution is provided in Appendix C and only some main aspects of them are discussed here. The turbulent buoyancy flux contribution, $w_{\mathrm{e}}^{\mathrm{tur}}$, is proportional to the turbulent buoyancy flux $-\langle w'b' \rangle_{z_{\mathrm{i}}}$. The sedimentation buoyancy flux contribution, $w_{\mathrm{e}}^{\mathrm{sed}}$, is proportional to the sedimentation buoyancy flux $\langle \mathbf{j}_\mu g \cdot \mathbf{k} \rangle_{z_{\mathrm{i}}}$ (see section 2.1). The evaporative cooling contribution, $w_{\mathrm{e}}^{\mathrm{eva}}$, is proportional to $E_0 - \langle E \rangle_{z_{\mathrm{i}}}$, the difference between the net (or integrated or accumulated) evaporative cooling across the whole cloud top region

$$E_0 = \int_{z_{-\infty}}^{z_\infty} \langle s^{\mathrm{eva}} \rangle \mathrm{d}z \tag{15}$$

and the integrated evaporative cooling up to z_{i}, $\langle E \rangle_{z_{\mathrm{i}}} = \int_{z_{-\infty}}^{z_{\mathrm{i}}} \langle s^{\mathrm{eva}} \rangle \mathrm{d}z$. Likewise, the radiative contribution, $w_{\mathrm{e}}^{\mathrm{rad}}$, is proportional to $\beta(R_0 - \langle R \rangle_{z_{\mathrm{i}}})$, the difference of the net radiative flux above the cloud top, R_0, and its value at z_{i}, $\langle R \rangle_{z_{\mathrm{i}}}$, where the parameter β accounts for condensational warming effects (cf. section 2.1). Furthermore, $w_{\mathrm{e}}^{\mathrm{mol}}$ denotes the molecular flux contributions and $w_{\mathrm{e}}^{\mathrm{def}}$ the deformation contribution, where the latter describes temporal changes in the shape of the mean buoyancy profile. In the subsequent analysis, all contributions to the mean entrainment velocity w_{e} are normalized by the reference entrainment velocity scale $W_{\mathrm{ref}} = \beta B_0 / \Delta b$, which is $W_{\mathrm{ref}} \simeq 4$ mm/s for RF01 of the DYCOMS-II field campaign considered here.

Before discussing the combined effect of droplet sedimentation and wind shear on the mean entrainment velocity, we need to elaborate on three aspects. First, although the net evaporative and radiative cooling rates are commensurate with each other (E_0 approximately varies between $0.5\,\beta B_0$ and $1.5\,\beta B_0$ for all cases considered in this study), the vertical distribution of those cooling rates varies substantially with height. As observed in Figure 4, the profile of the evaporative cooling rate $\langle s^{\mathrm{eva}} \rangle$ concentrates around the EIL whereas the profile of the radiative cooling rate $\langle s^{\mathrm{rad}} \rangle$ penetrates deeper in the cloud. Hence, the evaporative cooling contribution to the mean entrainment velocity is significantly larger than the radiative contribution for the reference heights that we use in this study, where we focus on the EIL, but this should not be interpreted as radiative cooling effects being negligible.

Second, the simulated entrainment velocities agree well with measurements. According to Figure 5 the quasi-steady entrainment velocity is approximately 4.5 mm/s and is thus commensurate with measurements of RF01 of DYCOMS-II, which report entrainment velocities in the range of 3.9–4.7mm/s (Faloona et al., 2005; Stevens et al., 2003). The quasi-steady entrainment velocity $w_{\mathrm{e}} - w_{\mathrm{e}}^{\mathrm{def}} = w_{\mathrm{e}}^{\mathrm{tur}} + w_{\mathrm{e}}^{\mathrm{sed}} + w_{\mathrm{e}}^{\mathrm{eva}} + w_{\mathrm{e}}^{\mathrm{rad}} + w_{\mathrm{e}}^{\mathrm{mol}}$ ignores unsteady effects (characterized by $w_{\mathrm{e}}^{\mathrm{def}}$) and thus characterizes the cloud in a quasi-steady state, which is by definition a state where $w_{\mathrm{e}}^{\mathrm{def}}$ is small compared to $w_{\mathrm{e}}^{\mathrm{tur}} + w_{\mathrm{e}}^{\mathrm{sed}} + w_{\mathrm{e}}^{\mathrm{eva}} + w_{\mathrm{e}}^{\mathrm{rad}} + w_{\mathrm{e}}^{\mathrm{mol}}$ (Schulz & Mellado, 2018). Measurements campaigns are often performed within a quasi-steady state, and therefore, the quasi-steady entrainment velocity is used for comparison. An additional advantage of using the quasi-steady entrainment velocity is that its magnitude is insensitive toward the choice of the reference height z_{i}, even though the individual entrainment velocity contributions can depend strongly on the choice of the reference height z_{i} as elucidated in Schulz and Mellado (2018).

Third, previous work by de Lozar and Mellado (2017) and Schulz and Mellado (2018) has shown that changes of w_{e} with droplet sedimentation and wind shear separately, that is, $\partial w_{\mathrm{e}} / \partial u_{\mathrm{sed}}$ and $\partial w_{\mathrm{e}} / \partial \Delta u$, show little dependence on the low-to-moderate Reynolds numbers of the simulations, even though the magnitude of the molecular flux contribution $w_{\mathrm{e}}^{\mathrm{mol}}$ can be comparable with the turbulent buoyancy flux contribution $w_{\mathrm{e}}^{\mathrm{tur}}$.

4.2. Competing Effects of Droplet Sedimentation and Wind Shear on w_{e}

Figure 5 shows that entrainment reduction by droplet sedimentation can completely compensate entrainment enhancement by wind shear. While droplet sedimentation weakens the quasi-steady entrainment velocity $w_{\mathrm{e}} - w_{\mathrm{e}}^{\mathrm{def}}$ by approximately 0.2–0.3 W_{ref} for $Sv_0 = 0.043$ and by 0.4–0.6 W_{ref} for $Sv_0 = 0.1$, with the

interval indicating the dependence on the shear strength, a strong wind shear with $Sh_0 = 10$ does the opposite and enhances the quasi-steady entrainment velocity $w_e - w_e^{def}$ by approximately 0.3–0.4 W_{ref}, with the interval indicating the dependence on the sedimentation strength. However, note that entrainment reduction by droplet sedimentation can only partly compensate entrainment enhancement by wind shear if the cloud top velocity jumps significantly exceeds $Sh_0 = 10$ (see discussion in section 2.2). In addition, Figure 5 shows that droplet sedimentation and wind shear interact to a good approximation in an multiplicative way. For instance, strong sedimentation alone decreases w_e approximately by a factor of 0.6, while a strong shear alone increases w_e approximately by a factor of 1.4. This result suggests that combining sedimentation and shear would change w_e approximately by a factor of $1.4 \times 0.6 = 0.84$, and indeed, Figure 5 reveals a factor of 0.8. (Although not shown, the same is true for the net evaporative cooling contribution E_0.) This multiplicative property might be useful for entrainment velocity parametrizations.

The preceding discussion indicates that sedimentation effects on the shear enhancement of entrainment remain moderate, namely, increasing the shear strength to $Sh_0 = 10$ increases the quasi-steady entrainment velocity $w_e - w_e^{def}$ by approximately 40% for $Sv_0 \leq 0.043$ and by approximately 30% for $Sv_0 = 0.1$. Likewise, shear effects on the sedimentation weakening of entrainment are negligible to leading order, namely, $w_e - w_e^{def}$ decreases by approximately 20% if the sedimentation strength is increased to $Sv_0 = 0.043$ and by approximately 40% if increased to $Sv_0 = 0.1$ irrespective of the imposed shear strength. In addition, Figure 5 demonstrates that a moderate wind shear with $Sh_0 = 5$ does not enhance the quasi-steady entrainment velocity, which confirms the critical cloud top velocity jump $(\Delta u)_{crit}$ discussed in section 3.2. All this suggests that if the shear enhancement is assumed to be linear within the range of Δu considered here, a shear on the order of $Sh_0 = 8$–9 (i.e., $\Delta u \simeq 2.4$–2.7 m/s for RF01 of DYCOMS-II) is needed to compensate the sedimentation-induced decrease of w_e associated with $Sv_0 = 0.043$, while a shear on the order of $Sh_0 = 12$–13 (i.e., $\Delta u \simeq 3.6$–3.9 m/s for RF01 of DYCOMS-II) is needed to compensate the sedimentation-induced decrease of w_e associated with $Sv_0 = 0.1$.

4.3. Contributions to w_e From Different Cloud Top Processes

The various contributions to the mean entrainment velocity change with sedimentation and shear as indicated in Figure 6. Sedimentation and shear mainly alter two of the six contributions of the entrainment rate equation, equation (14), namely, the turbulent buoyancy flux contribution w_e^{tur} and the evaporative cooling contribution w_e^{eva}. In contrast, changes in the sedimentation buoyancy flux contribution w_e^{sed} and in the radiative cooling contribution w_e^{rad} are less important. The subsequent analysis focuses on the joint effect of sedimentation and shear on these four contributions. A thorough discussion of w_e^{mol} and w_e^{def} can be found in Schulz and Mellado (2018) and will not be further developed here.

Droplet sedimentation effects can partly compensate wind shear enhancement of the turbulent buoyancy flux contribution w_e^{tur}. While a sufficiently strong wind shear with $\Delta u > (\Delta u)_{crit}$ substantially enhances the turbulent buoyancy flux contribution w_e^{tur} by amplifying the mixing of free-tropospheric and cloudy air, droplet sedimentation does the opposite and substantially weakens w_e^{tur} by thickening the EIL, which weakens the shear production term and thus the turbulent buoyancy flux around $z_{i,f}$ (see Figures 6a and 6b and discussion in section 3.2). For the shear-free case droplet sedimentation does not alter w_e^{tur}. Moreover, the magnitude of w_e^{tur} and thus the importance of sedimentation and shear effects on w_e^{tur} depend strongly on the choice of the reference height z_i. For reference heights near $z_{i,f}$ considering sedimentation and shear effects on w_e^{tur} is key, while considering sedimentation and shear effects on w_e^{tur} is less important for reference heights near $z_{i,n}$ as w_e^{tur} is small at those reference heights.

We further find that droplet sedimentation and wind shear effects on the evaporative cooling contribution w_e^{eva} can completely compensate each other. While droplet sedimentation removes cloudy air from the EIL, which prevents cloud droplets from evaporating and thus weakens w_e^{eva}, a strong wind shear does the opposite and amplifies the mixing of environmental and cloudy air, which enhances evaporation in the EIL and thus enhances w_e^{eva} (e.g., Ackerman et al., 2004, 2009; Bretherton et al., 2007; de Lozar & Mellado, 2017; Mellado et al., 2014; Schulz & Mellado, 2018). This compensating effect of sedimentation and shear on w_e^{eva} is especially important for reference heights located near $z_{i,n}$ since w_e^{eva} is the dominant contribution to the mean entrainment velocity w_e for such reference heights. (w_e^{eva} decays rapidly for reference heights above $z_{i,n}$, and w_e^{tur} is equally or more important than w_e^{eva} at $z_{i,f}$.) Particularized to $z_{i,n}$, Figures 6c and 6d show that imposing a strong sedimentation flux with $Sv_0 = 0.1$ weakens w_e^{eva} by approximately 40%, while imposing a strong shear with $Sh_0 = 10$ amplifies w_e^{eva} by approximately 40%. Figures 6c and 6d further show that the

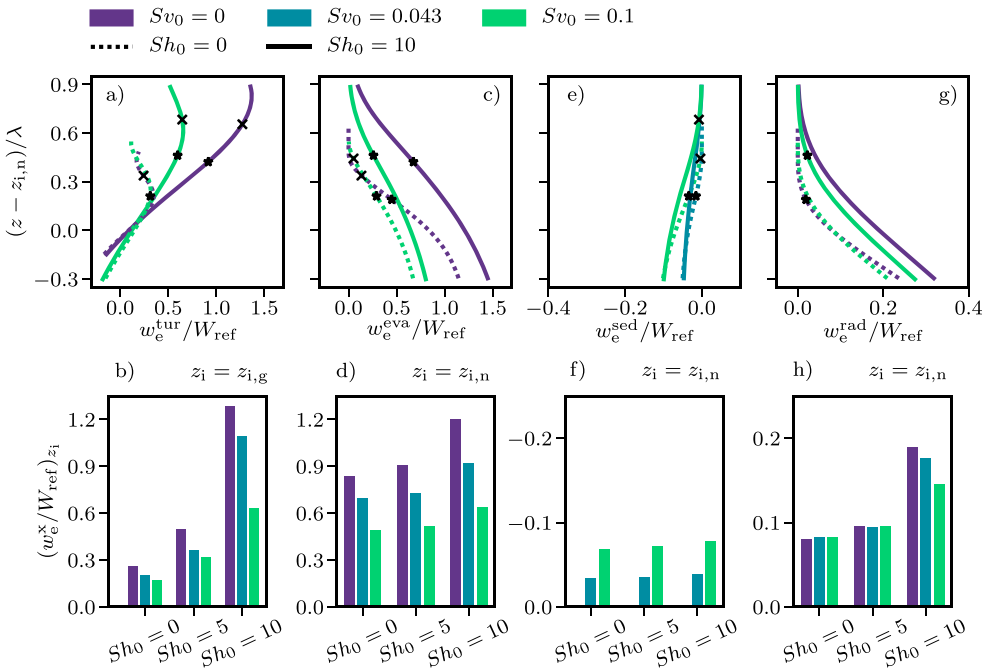

Figure 6. Different contributions to the mean entrainment velocity w_e according to equation (14), where the top row presents vertical profiles and the bottom row presents normalized values calculated at the reference height z_i. The stars and crosses in the top row indicate the height of minimum turbulent buoyancy flux $z_{i,f}$ and the height of the maximum gradient of the mean buoyancy profile $z_{i,g}$ respectively. The vertical distance z is plotted with respect to the height of zero mean buoyancy $z_{i,n}$. (a, b) Normalized turbulent buoyancy flux contribution $w_e{}^{tur}/W_{ref}$, (c, d) normalized evaporative contribution w_e^{eva}/W_{ref}, (e, f) normalized sedimentation buoyancy flux contribution w_e^{sed}/W_{ref}, and (g, h) normalized radiative contribution w_e^{rad}/W_{ref}. Note the different vertical scales in panels (b,d) and (f,h). The figure is presented for $Re_0 = 400$ at $z_*/\lambda \simeq 11$.

sedimentation weakening of w_e^{eva} is to leading order independent of shear and that the shear enhancement of w_e^{eva} is to leading order independent of sedimentation. This indicates that coupling processes between sedimentation weakening and shear enhancement of w_e^{eva} remain moderate.

Removing cloudy air from the EIL does not only weaken evaporative cooling but does also promote an upward sedimentation buoyancy flux that directly opposes entrainment (see section 2.1), and the sedimentation buoyancy flux contribution w_e^{sed} is therefore a negative contribution to w_e in equation (14). The sedimentation buoyancy flux contribution w_e^{sed} is most important for reference heights near $z_{i,n}$ as the liquid water specific humidity q_ℓ increases when lowering the reference heights toward $z_{i,n}$. For $Sv_0 = 0.1$ the sedimentation buoyancy flux contribution w_e^{sed} at $z_{i,n}$ approximately contributes 0.1 W_{ref} to the overall sedimentation reduction of $w_e - w_e^{def}$ which is 0.4–0.6 W_{ref} according to Figure 5, where the interval indicates the dependence on shear. Since the magnitude of w_e^{sed} is nearly shear independent, this indicates that w_e^{sed} is more important in the absence of shear. Moreover, this shows that even though the magnitude of w_e^{sed} is small compared to w_e^{tur} and w_e^{eva}, it is an ~20% contribution to the overall sedimentation reduction of $w_e - w_e^{def}$ at $z_{i,n}$.

Regarding their effect on the radiative cooling contribution w_e^{rad}, we observe that droplet sedimentation and wind shear can partly compensate each other as well (Figures 6g and 6h). While sedimentation removes liquid water from the EIL, which weakens w_e^{rad}, shear does the opposite and puts additional liquid water into the EIL, which enhances w_e^{rad}. In any case, the magnitude of the radiative cooling contribution is small compared to w_e^{tur} and w_e^{eva} (note the different vertical scale in Figure 6h) and therefore quantifying sedimentation and shear effects on w_e^{rad} has no priority for atmospheric conditions similar to RF01 of DYCOMS-II. However, we emphasize once more that the net radiative cooling (i.e., integrated across the whole CTML) remains comparable to the net evaporative cooling for all sedimentation and shear numbers investigated, as discussed in section 4.1.

5. Summary and Conclusion

DNSs of the stratocumulus cloud top have been employed to show that droplet sedimentation and wind shear effects on cloud top entrainment can completely compensate each other for subtropical conditions with cloud top velocity jumps on the order of $\Delta u \simeq 3$ m/s. To better understand this compensation, droplet sedimentation and wind shear effects have been analyzed by means of an integral analysis of the buoyancy equation, which allows us to analytically decompose the mean entrainment velocity $w_e = \mathrm{d}z_i/\mathrm{d}t$ into contributions from turbulent mixing, w_e^{tur}, evaporative cooling, w_e^{eva}, droplet sedimentation, w_e^{sed}, and radiative cooling, w_e^{rad}. We observe that droplet sedimentation and wind shear mainly alter w_e^{tur} and w_e^{eva}. Wind shear amplifies the turbulent buoyancy flux contribution w_e^{tur} by amplifying the mixing of free tropospheric and cloudy air, while droplet sedimentation weakens the wind shear enhancement of w_e^{tur} by broadening the EIL, which causes a weakening of w_e^{tur}. In addition, wind shear enhanced mixing of free-tropospheric and cloudy air amplifies w_e^{eva}, while droplet sedimentation does the opposite and weakens w_e^{eva} by removing cloudy air from the EIL, which prevents cloud droplets from evaporating. Sedimentation- and shear-induced changes of w_e^{sed} and w_e^{rad} are small, meaning that they contribute less than 10-20% to the overall effect of sedimentation and shear on w_e. Note, however, that w_e^{rad} can become more important under different thermodynamic conditions, for example., weakening the jump in total water specific humidity is expected to increase the importance of radiative cooling compared to evaporative cooling (e.g., de Lozar & Mellado, 2015a). In sum, all this shows that sedimentation and shear effects on w_e primarily cancel each other due to their opposing effect on w_e^{tur} and w_e^{eva}.

The importance of the two compensating mechanisms introduced in the previous paragraph strongly depends on the choice of the reference height z_i where w_e^{tur} and w_e^{eva} are calculated, even though different definitions of the reference height z_i typically differ only by a few meters. For instance, for reference heights near to the height of zero mean buoyancy $z_{i,n}$ (the base of the capping inversion), the sedimentation weakening of w_e is primarily caused by changes in w_e^{eva}, while for reference heights near to the height of minimum turbulent buoyancy flux $z_{i,f}$, the sedimentation weakening of w_e is primarily caused by changes in w_e^{tur} and to a lesser degree by changes w_e^{eva}. All this shows that entrainment rate parametrizations should estimate contributions from different processes at the same reference height.

We further find that the sedimentation weakening of the entrainment velocity w_e is nearly shear independent, while the shear enhancement of the entrainment velocity w_e can moderately depend on sedimentation as sedimentation weakens the turbulent buoyancy flux contribution w_e^{tur} for a strongly sheared cloud top. For instance, a strong sedimentation with a bulk sedimentation velocity of $u_{sed} \simeq 30$ mm/s weakens the mean entrainment velocity by approximately 40% irrespectively of the imposed shear strength, while imposing a wind shear characterized by a cloud top velocity jump of $\Delta u \simeq 3$ m/s enhances w_e by approximately 40% for a moderate sedimentation with $u_{sed} \simeq 13$ mm/s and by approximately 30% for a strong sedimentation with $u_{sed} \simeq 30$ mm/s at the height of zero mean buoyancy $z_{i,n}$.

Last but not the least, we also find that, even in the presence of droplet sedimentation, wind shear enhancement of w_e is only observed once the cloud top velocity jump Δu exceeds its critical value $(\Delta u)_{crit}$, as obtained previously without droplet sedimentation (Schulz & Mellado, 2018). We find $(\Delta u)_{crit} \simeq 4$–$5 w_* \simeq 1$–$4$ m/s for typical values of the convective velocity scale $w_* \simeq 0.2$–0.9 m/s (Wood, 2012), where variations in the prefactor of w_* characterize droplet sedimentation effects. This shows that droplet sedimentation effects on $(\Delta u)_{crit}$ remain moderate (below 25%), which indicates that $(\Delta u)_{crit}$ remains a useful quantity for characterizing wind shear effects even in the case of strong droplet sedimentation.

In summary, this work demonstrates that the mean entrainment velocity can be equally sensitive toward changes in the sedimentation strength and toward changes in cloud top wind shear. This result implies that entrainment parametrizations should pay equal attention to droplet sedimentation and to wind shear effects. Besides, this result implies that the droplet size distribution can substantially affect cloud lifetimes not only because of its effect on rain formation but also because of its effect on cloud top entrainment, which emphasizes the importance of precise measurements of the droplet size distribution and of appropriate representations of it in numerical models.

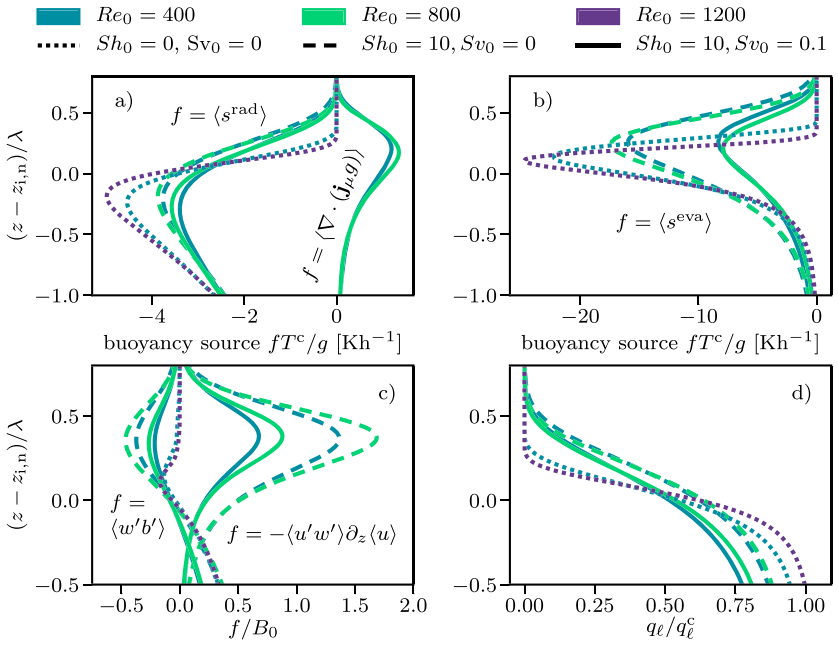

Figure A1. (a, b) The different buoyancy source terms (cf. Figure 4) according to equation (13). (c) The normalized turbulent buoyancy flux and the normalized shear production term (cf. Figure 3). (d) The normalized liquid water specific humidity. Different colors indicate different Reynolds numbers, and different line styles indicate different sedimentation and shear numbers. Besides, all presented plots are averaged over the period $7.5 < z_*/\lambda < 8.5$ (cf. Table 1).

Appendix A: Reynolds Number Effects

Reynolds number effects for sedimentation alone and for shear alone are observed to be less than 20% when increasing the Reynolds number by a factor of 2 in de Lozar and Mellado (2017) and by a factor of up to 3 in Schulz and Mellado (2018), respectively. A detailed discussion of Reynolds number effects is given in (Mellado et al., 2018; Schulz & Mellado, 2018) and here we only analyze three cases, namely, $\{Sh_0 = 0, Sv_0 = 0.0\}$, $\{Sh_0 = 10, Sv_0 = 0.0\}$, and $\{Sh_0 = 10, Sv_0 = 0.1\}$. Figure A1 shows that for those three cases most presented quantities vary by less than 20% when increasing the Reynolds numbers by a factor of up to 3. A notable exception is that the shear production term $P = -\langle u'w' \rangle \partial_z \langle u \rangle$ varies by up to 50% (corresponding to $0.3B_0$) when doubling the Reynolds number for the case $\{Sh_0 = 10, Sv_0 = 0.1\}$. However, despite this large number, the relative change of the shear production term P with sedimentation, that is, how the difference $P_{Sh_0=10,Sv_0=0.0} - P_{Sh_0=10,Sv_0=0.1}$ changes with Re_0, varies by less than 10% with when doubling the Reynolds number. This indicates that our low-to-moderate Reynolds number simulations adequately represent sedimentation effects on the shear production term. Reynolds number effects on the net evaporative cooling E_0 and on the normalized quasi-steady entrainment velocity $[(w_e - w_e^{def})/W_{ref}]_{z_{i,n}}$ are not presented in Figure A1 but are also found to be below 20% for the three analyzed cases. This tendency toward Reynolds number similarity is a general characteristic of turbulent flows (Dimotakis, 2005; Mellado et al., 2018) and allows us to partly extrapolate our results to atmospheric conditions.

Appendix B: Sedimentation and Shear Effects on the EIL Thickness

The derivation of the critical cloud top velocity jump $(\Delta u)_{crit}$ introduced in section 3.2 is based on the observation that the EIL thickness h_{EIL} is scaled by two different length scales, namely, the penetration depth δ and the shear layer thickness h_S. Details of the derivation can be found in Schulz and Mellado (2018) and in the following we only discuss the combined effect of sedimentation and shear on these two scalings of the EIL thickness.

First, h_{EIL} is scaled by the sum of the penetration depth δ and the diffusive thickness h_{diff} as indicated in Figure B1a. The penetration depth δ characterizes the depth that in-cloud turbulent convection can penetrate into the stably stratified EIL and is defined as twice the difference between the height of minimum

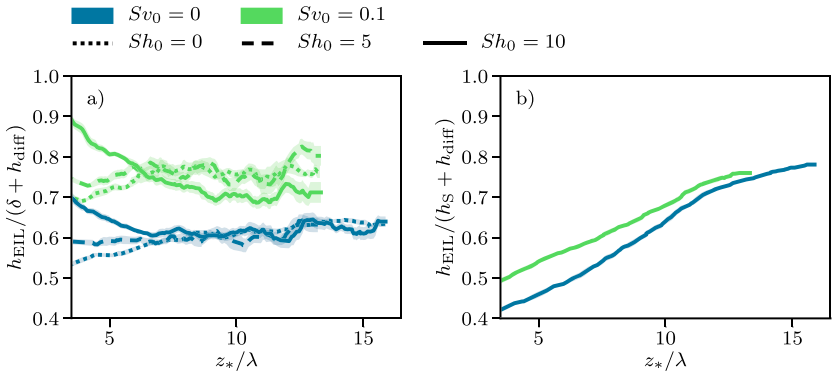

Figure B1. (a) The entrainment interfacial layer (EIL) thickness h_{EIL} normalized by the sum of the penetration depth δ and the diffusive thickness h_{diff}. (b) h_{EIL} normalized by the sum of the critical shear layer thickness h_S and the diffusive thickness h_{diff}. Shaded areas indicate two standard deviations around the mean. The figure is presented for $Re_0 = 400$.

turbulent buoyancy flux $z_{i,f}$ and the height of zero mean buoyancy $z_{i,n}$, that is,

$$\delta = 2(z_{i,f} - z_{i,n}) \, . \tag{B1}$$

The diffusive thickness h_{diff} accounts for low-to-moderate Reynolds number artifacts as elucidated in detail in de Lozar & Mellado (2015b), Mellado et al. (2010), and Schulz & Mellado (2018). Moreover, Figure B1a shows that sedimentation effects on the scaling of h_{EIL} with $\delta + h_{diff}$ are on the order of 20%, and this effect decreases as shear intensifies.

Second, for a sufficiently strong shear h_{EIL} is scaled by the sum of the critical shear layer thickness h_S and the diffusive thickness h_{diff} as indicated in Figure B1b. The critical shear layer thickness h_S characterizes the vertical extent of wind shear effects and is defined according to Mellado et al. (2014) as

$$h_S = \frac{(\Delta u)^2}{3\Delta b} \, , \tag{B2}$$

where the subscript "S" indicates shear. Figure B1b shows that sedimentation effects on the scaling $h_{EIL}/(h_S + h_{diff})$ are less than 10%, which indicates that those effects are negligible to leading order.

Appendix C: The Entrainment Rate Equation

The buoyancy evolution equation (see equation 13), as explained in de Lozar and Mellado (2015b, 2017), can be written as

$$\mathrm{D}_t b = \kappa_T \nabla^2 b + s^{rad} + s^{eva} + \nabla \cdot (\mathbf{j}_\mu g) + C(\epsilon) \, , \tag{C1}$$

where κ_T is the thermal diffusivity and the radiative and evaporative source terms are defined as

$$s^{rad} = \left[1 - \frac{\beta_l q_\ell^c}{\psi_{sat}} \right] \frac{g \nabla \cdot \mathbf{R}}{c_p^c T^c} \quad \text{and} \tag{C2}$$

$$s^{eva} = g \beta^\ell q_\ell^c \left[\frac{-(\partial_t q_\ell)_{pha}}{q_\ell^c} + \frac{d_\xi f \nabla \cdot \mathbf{R}}{\psi_{sat} \quad c_p^c T^c} \right] \, . \tag{C3}$$

The parameter ψ_{sat} quantifies radiative effects at saturation conditions and β^ℓ specifies phase change effects of the buoyancy. Due to condensational warming, only a part β of the radiatively induced enthalpy changes translates into buoyancy changes, where β is given by $\beta = (1 - \beta^\ell q_\ell^c \psi_{sat}^{-1}) \simeq 0.53$ and condensational warming is also the origin of the second summand in equation (C3). Besides, $\mathbf{R} = R\mathbf{k}$ is the one-dimensional longwave radiative forcing based on Larson et al. (2007), with $\mathbf{k}$ being a unit vector pointing in the vertical direction. The net longwave radiative flux $R = R(z)$ can be well approximated by

$R = R_0 \exp\left[-\lambda^{-1}\int_z^{z_{\text{top}}} q_\ell / q_\ell^{\text{c}} \mathrm{d}z'\right]$, where R_0 is the net radiative flux cooling the cloud top region and λ is the extinction length. The sedimentation buoyancy flux $\mathbf{j}_\mu$ is defined in equation (2). The function $C(\epsilon)$ is a correction factor that results from the smoothing of the liquid function $\ell(\xi, \epsilon)$ as discussed in de Lozar and Mellado (2017). In the limit $\epsilon \to 0$ the correction term vanishes; however, $\epsilon = 1/16$ produces a small integrated correction term equal to 10% of the sedimentation buoyancy flux [i.e., $\int C(1/16)\mathrm{d}V \sim 0.1\mathbf{j}_\mu g \cdot \mathbf{k}$].

The entrainment rate equation $w_{\text{e}} = w_{\text{e}}^{\text{tur}} + w_{\text{e}}^{\text{sed}} + w_{\text{e}}^{\text{eva}} + w_{\text{e}}^{\text{rad}} + w_{\text{e}}^{\text{mol}} + w_{\text{e}}^{\text{def}}$ (see equation (14)) is obtained by integrating the buoyancy evolution equation from an arbitrary reference height $z = z_{\text{i}}$ upward (see Mellado et al., 2018, for details). The single contributions are defined as follows:

$$w_{\text{e}}^{\text{tur}}(b^{\text{d}} - \langle b\rangle_{z_{\text{i}}}) = -\langle w'b'\rangle_{z_{\text{i}}} \tag{C4}$$

$$w_{\text{e}}^{\text{sed}}(b^{\text{d}} - \langle b\rangle_{z_{\text{i}}}) = \langle \mathbf{j}_\mu g \cdot \mathbf{k}\rangle_{z_{\text{i}}} \tag{C5}$$

$$w_{\text{e}}^{\text{eva}}(b^{\text{d}} - \langle b\rangle_{z_{\text{i}}}) = E_0 - \langle E\rangle_{z_{\text{i}}} \tag{C6}$$

$$w_{\text{e}}^{\text{rad}}(b^{\text{d}} - \langle b\rangle_{z_{\text{i}}}) = \beta g (c_p^{\text{c}} T^{\text{c}})^{-1}(R_0 - \langle R\rangle_{z_{\text{i}}}) \tag{C7}$$

$$w_{\text{e}}^{\text{mol}}(b^{\text{d}} - \langle b\rangle_{z_{\text{i}}}) = \kappa_{\text{T}} \partial_z \langle b\rangle_{z_{\text{i}}}\ , \tag{C8}$$

$$w_{\text{e}}^{\text{def}}(b^{\text{d}} - \langle b\rangle_{z_{\text{i}}}) = -\frac{\mathrm{d}}{\mathrm{d}t}\int_{z_{\text{i}}}^{z_\infty} (b^{\text{d}} - \langle b\rangle(z))\mathrm{d}z. \tag{C9}$$

Acknowledgments
The authors gratefully acknowledge the Gauss Centre for Supercomputing e.V. (www.gauss-centre.eu) for funding this project by providing computing time through the John von Neumann Institute for Computing (NIC) on the GCS Supercomputer JUWELS at Jülich Supercomputing Centre (JSC). Funding was provided by the Max Planck Society through its Max Planck Research Groups program. Primary data used in the analysis and other supporting information that may be useful in reproducing the author's work are available online (http://cera-www.dkrz.de/WDCC/ui/Compact.jsp?acronym=DKRZ_LTA_738_ds00003).

References

Ackerman, A. S., Kirkpatrick, M. P., Stevens, D. E., & Toon, O. B. (2004). The impact of humidity above stratiform clouds on indirect aerosol climate forcing. *Nature*, *432*(7020), 1014.

Ackerman, A. S., VanZanten, M. C., Stevens, B., Savic-Jovcic, V., Bretherton, C. S., Chlond, A., et al. (2009). Large-eddy simulations of a drizzling, stratocumulus-topped marine boundary layer. *Monthly Weather Review*, *137*(3), 1083–1110.

Bailon-Cuba, J., Emran, M. S., & Schumacher, J. (2010). Aspect ratio dependence of heat transfer and large-scale flow in turbulent convection. *Journal of Fluid Mechanics*, *655*, 152–173.

Bretherton, C., Blossey, P. N., & Uchida, J. (2007). Cloud droplet sedimentation, entrainment efficiency, and subtropical stratocumulus albedo. *Geophysical Research Letters*, *34*, L03813. https://doi.org/10.1029/2006GL027648

Brost, R., Wyngaard, J., & Lenschow, D. (1982). Marine stratocumulus layers. Part II: Turbulence budgets. *Journal of the Atmospheric Sciences*, *39*(4), 818–836.

Caughey, S., Crease, B., & Roach, W. (1982). A field study of nocturnal stratocumulus II. Turbulence structure and entrainment. *Quarterly Journal of the Royal Meteorological Society*, *108*(455), 125–144.

de Lozar, A., & Mellado, J. (2014). Cloud droplets in a bulk formulation and its application to buoyancy reversal instability. *Quarterly Journal of the Royal Meteorological Society*, *140*, 1493–1504.

de Lozar, A., & Mellado, J. P. (2015a). Evaporative cooling amplification of the entrainment velocity in radiatively driven stratocumulus. *Geophysical Research Letters*, *42*, 7223–7229. https://doi.org/10.1002/2015GL065529

de Lozar, A., & Mellado, J. P. (2015b). Mixing driven by radiative and evaporative cooling at the stratocumulus top. *Journal of the Atmospheric Sciences*, *72*(12), 4681–4700.

de Lozar, A., & Mellado, J. P. (2017). Reduction of the entrainment velocity by cloud droplet sedimentation in stratocumulus. *Journal of the Atmospheric Sciences*, *74*(3), 751–765.

de Roode, S. R., & Wang, Q. (2007). Do stratocumulus clouds detrain? FIRE I data revisited. *Boundary-layer meteorology*, *122*(2), 479–491.

Deardorff, J. W. (1980a). Stratocumulus-capped mixed layers derived from a three-dimensional model. *Boundary-Layer Meteorology*, *18*(4), 495–527.

Deardorff, J. (1980b). Cloud top entrainment instability. *Journal of the Atmospheric Sciences*, *37*(1), 131–147.

Dimotakis, P. E. (2005). Turbulent mixing. *Annual Review of Fluid Mechanics*, *37*, 329–356.

Driedonks, A., & Duynkerke, P. (1989). Current problems in the stratocumulus-topped atmospheric boundary layer. *Boundary-Layer Meteorology*, *46*(3), 275–303.

Faloona, I., Lenschow, D. H., Campos, T., Stevens, B., Van Zanten, M., Blomquist, B., et al. (2005). Observations of entrainment in eastern Pacific marine stratocumulus using three conserved scalars. *Journal of the Atmospheric Sciences*, *62*(9), 3268–3285.
Gerber, H., Frick, G., Malinowski, S., Brenguier, J., & Burnet, F. (2005). Holes and entrainment in stratocumulus. *Journal of the Atmospheric Sciences*, *62*(2), 443–459.
Gerber, H., Malinowski, S. P., & Jonsson, H. (2016). Evaporative and radiative cooling in POST Stratocumulus. *Journal of the Atmospheric Sciences*, *73*(10), 3877–3884.
Glienke, S., Kostinski, A., Fugal, J., Shaw, R., Borrmann, S., & Stith, J. (2017). Cloud droplets to drizzle: Contribution of transition drops to microphysical and optical properties of marine stratocumulus clouds. *Geophysical Research Letters*, *44*, 8002–8010. https://doi.org/10.1002/2017GL074430
Grosvenor, D. P., Sourdeval, O., Zuidema, P., Ackerman, A., Alexandrov, M. D., Bennartz, R., et al. (2018). Remote sensing of droplet number concentration in warm clouds: A review of the current state of knowledge and perspectives. *Reviews of Geophysics*, *56*, 409–453. https://doi.org/10.1029/2017RG000593
Haman, K. E., Malinowski, S. P., Kurowski, M. J., Gerber, H., & Brenguier, J.-L. (2007). Small scale mixing processes at the top of a marine stratocumulus—A case study. *Quarterly Journal of the Royal Meteorological Society*, *133*(622), 213–226.
Hill, A. A., Feingold, G., & Jiang, H. (2009). The influence of entrainment and mixing assumption on aerosol-cloud interactions in marine stratocumulus. *Journal of the Atmospheric Sciences*, *66*(5), 1450–1464.
Hudson, J. G., & Yum, S. S. (1997). Droplet spectral broadening in marine stratus. *Journal of the Atmospheric Sciences*, *54*(22), 2642–2654.
Jen-La Plante, I., Ma, Y., Nurowska, K., Gerber, H., Khelif, D., Karpinska, K., et al. (2016). Physics of Stratocumulus Top (POST): Turbulence characteristics. *Atmospheric Chemistry and Physics*, *16*(15), 9711–9725.
Katzwinkel, J., Siebert, H., & Shaw, R. (2012). Observation of a self-limiting, shear-induced turbulent inversion layer above marine stratocumulus. *Boundary-Layer Meteorology*, *145*(1), 131–143.
Kopec, M. K., Malinowski, S. P., & Piotrowski, Z. P. (2016). Effects of wind shear and radiative cooling on the stratocumulus-topped boundary layer. *Quarterly Journal of the Royal Meteorological Society*, *142*(701), 3222–3233.
Larson, V. E., Kotenberg, K. E., & Wood, N. B. (2007). An analytic longwave radiation formula for liquid layer clouds. *Monthly Weather Review*, *135*(2), 689–699.
Lele, S. K. (1992). Compact finite difference schemes with spectral-like resolution. *Journal of Computational Physics*, *103*(1), 16–42.
Lilly, D. K. (1968). Models of cloud-topped mixed layers under a strong inversion. *Quarterly Journal of the Royal Meteorological Society*, *94*(401), 292–309.
Malinowski, S., Gerber, H., Plante, J.-L., Kopec, M., Kumala, W., Nurowska, K., et al. (2013). Physics of Stratocumulus Top (POST): Turbulent mixing across capping inversion. *Atmospheric Chemistry and Physics*, *13*(24), 12,171–12,186.
Martin, G., Johnson, D., & Spice, A. (1994). The measurement and parameterization of effective radius of droplets in warm stratocumulus clouds. *Journal of the Atmospheric Sciences*, *51*(13), 1823–1842.
Mellado, J. P. (2010). The evaporatively driven cloud-top mixing layer. *Journal of Fluid Mechanics*, *660*, 5–36.
Mellado, J. P. (2012). Direct numerical simulation of free convection over a heated plate. *Journal of Fluid Mechanics*, *712*, 418–450.
Mellado, J. P. (2017). Cloud-top entrainment in stratocumulus clouds. *Annual Review of Fluid Mechanics*, *49*, 145–169.
Mellado, J. P., & Ansorge, C. (2012). Factorization of the Fourier transform of the pressure-Poisson equation using finite differences in colocated grids. *ZAMM-Journal of Applied Mathematics and Mechanics/Zeitschrift für Angewandte Mathematik und Mechanik*, *92*(5), 380–392.
Mellado, J.-P., Bretherton, C., Stevens, B., & Wyant, M. (2018). DNS and LES for simulating stratocumulus: Better together. *Journal of Advances in Modeling Earth Systems*, *10*, 1421–1438. https://doi.org/10.1029/2018MS001312
Mellado, J. P., Stevens, B., & Schmidt, H. (2014). Wind shear and buoyancy reversal at the top of stratocumulus. *Journal of the Atmospheric Sciences*, *71*(3), 1040–1057.
Mellado, J. P., Stevens, B., Schmidt, H., & Peters, N. (2010). Two-fluid formulation of the cloud-top mixing layer for direct numerical simulation. *Theoretical and Computational Fluid Dynamics*, *24*(6), 511–536.
Miles, N. L., Verlinde, J., & Clothiaux, E. E. (2000). Cloud droplet size distributions in low-level stratiform clouds. *Journal of the Atmospheric Sciences*, *57*(2), 295–311.
Nicholls, S., & Leighton, J. (1986). An observational study of the structure of stratiform cloud sheets: Part I. Structure. *Quarterly Journal of the Royal Meteorological Society*, *112*(472), 431–460.
Pawlowska, H., & Brenguier, J.-L. (2000). Microphysical properties of stratocumulus clouds during ACE-2. *Tellus B*, *52*(2), 868–887. https://doi.org/10.1034/j.1600-0889.2000.00076.x
Randall, D. A. (1980). Conditional instability of the first kind upside-down. *Journal of the Atmospheric Sciences*, *37*(1), 125–130.
Schulz, B., & Mellado, J. P. (2018). Wind shear effects on radiatively and evaporatively driven stratocumulus tops. *Journal of the Atmospheric Sciences*, *75*(9), 3245–3263.
Stevens, B. (2005). Atmospheric moist convection. *Annual Review of Earth and Planetary Sciences*, *33*, 605–643.
Stevens, B., Lenschow, D. H., Faloona, I., Moeng, C.-H., Lilly, D., Blomquist, B., et al. (2003). On entrainment rates in nocturnal marine stratocumulus. *Quarterly Journal of the Royal Meteorological Society*, *129*(595), 3469–3493.
Stevens, B., Moeng, C.-H., Ackerman, A. S., Bretherton, C. S., Chlond, A., de Roode, S., et al. (2005). Evaluation of large-eddy simulations via observations of nocturnal marine stratocumulus. *Monthly Weather Review*, *133*(6), 1443–1462.
VanZanten, M., Stevens, B., Vali, G., & Lenschow, D. (2005). Observations of drizzle in nocturnal marine stratocumulus. *Journal of the Atmospheric Sciences*, *62*(1), 88–106.
Wang, S., Golaz, J.-C., & Wang, Q. (2008). Effect of intense wind shear across the inversion on stratocumulus clouds. *Geophysical Research Letters*, *35*, L15814. https://doi.org/10.1029/2008GL033865
Wang, S., Zheng, X., & Jiang, Q. (2012). Strongly sheared stratocumulus convection: An observationally based large-eddy simulation study. *Atmospheric Chemistry and Physics*, *12*(11), 5223–5235.
Wood, R. (2000). Parametrization of the effect of drizzle upon the droplet effective radius in stratocumulus clouds. *Quarterly Journal of the Royal Meteorological Society*, *126*(570), 3309–3324.
Wood, R. (2012). Stratocumulus clouds. *Monthly Weather Review*, *140*(8), 2373–2423.